JOURNAL OF THERMOPHYSICS AND HEAT TRANSFER
Vol. 22, No. 1, January–March 2008

Performance Characteristics of Electrohydrodynamic Conduction Pump in Two-Phase Loops

Seong-Il Jeong*
Korea Advanced Institute of Science and Technology, Daejeon 305-701, Republic of Korea
and
Jeffrey Didion†
NASA Goddard Space Flight Center, Greenbelt, Maryland 20771

DOI: 10.2514/1.23680

A direct-current electric field applied to dielectric fluids causes an imbalance in the dissociation-recombination reaction generating free space charges. Coulomb forces, resulting from the applied electric field, redistributes the generated charges resulting in the heterocharge layers in the vicinity of the electrodes. Proper design of the electrodes generates net axial flow motion pumping the fluid. The electrohydrodynamic conduction pump is a novel device that pumps dielectric fluids using heterocharge layers formed by imposition of electrostatic fields. This paper investigates the performance characteristics of an electrohydrodynamic conduction pump in two-phase (liquid-vapor) thermal control loops. The electrohydrodynamic two-phase loop consists of an electrohydrodynamic conduction pump, condenser, evaporator, transport lines, and reservoir (accumulator). This paper presents the results of an extensive experimental matrix examining the operational performance of electrohydrodynamic-based two-phase loops. The testing programs employed two electrohydrodynamic-based loops, two electrohydrodynamic conduction pumps, and deaerated and commercial grade HFC-134a. The pumps and fluids were alternated between the loops to provide a degree of generality to the results. We report the generated pressure head, mass flow rate, and pump power consumption as a function of refrigerant, applied voltage, and sink temperature. The experimental program lasted over two years. The experiments' results identified the effects of noncondensable gases, working fluid temperature, loop geometric parameter, and electrode design parameters to improve electrohydrodynamic conduction pump performance.

Nomenclature

A	=	cross section area of electrohydrodynamic pump section
C_p	=	specific heat at constant pressure
D_i	=	inner diameter of loop
E	=	electric field
f_e	=	electric body force density
G	=	mass velocity
h_{lv}	=	latent heat of vaporization
I	=	current
$\dot{m}$	=	mass flow rate
P	=	pressure
q	=	heat flux
q	=	net electric charge density
T	=	temperature
u	=	average flow velocity in electrohydrodynamic pump section
V	=	voltage
X	=	distance along evaporator
x	=	quality
ε	=	electric permittivity
ρ	=	fluid density
σ	=	electric conductivity
τ	=	charge relaxation time, $=\varepsilon/\sigma$

Subscript

in	=	inlet
sat	=	saturation

Presented as Paper 5069 at the 38th AIAA Thermophysics Conference, Toronto, Ontario, Canada, 6–9 June 2005; received 6 March 2006; revision received 28 June 2007; accepted for publication 4 July 2007.

*Senior Researcher, Satellite Technology Research Center, 373-1, Guseong-Dong, Yuseong-Gu.
†Senior Aerospace Engineer, Thermal Technology Development, Code 545.2.

Introduction

HEAT pipes, capillary pumped loops (CPLs), and loop heat pipes (LHPs) are two-phase heat transfer devices which transfer heat with little temperature difference by means of the capillary pressure head developed within the wick structure. Therefore, the capillary pumping capacity is the primary limitation governing the operation of these devices. Heat pipes, in particular, have very limited pumping capability. CPLs and LHPs have relatively high pumping capability; however, they have other difficulties such as unwarranted immediate startup and recovery from dryout. These devices generally require a 30–50 W starter-heater to enhance the chances of startup success [1]. Electrohydrodynamic (EHD) pumping is a promising candidate to assist capillary operations or replace these devices. EHD pumps offer engineering advantages, especially such as simple design, nonmechanical, low acoustic noise, lightweight, rapid control of performance, and low-power consumption, which are most attractive, particularly in a space environment that emphasizes conservation of mass, volume, and power consumption. Furthermore, EHD pumps provide immediate startup operation, prompt recovery from dryout, and feasibility of microscale application.

Several researchers report experimental investigations of heat pipes using EHD pumps to replace/assist capillary pumping [2–5]. Mo et al. [6] performed an experimental study to characterize the startup process for an EHD-assisted capillary pumped loop (CPL) system. Their experimental data showed that the EHD techniques can reduce the startup time by as much as 50% at an applied voltage of 10 kV at a power level of 10 W with HFC-134a as the working fluid. The startup time reduction for the 20 and 50 W power levels were 30 and 20%, respectively. Jeong and Didion [7] installed an

EHD conduction pump in a two-phase loop with high heat flux source and confirmed that the EHD conduction pump can be used as a stand-alone system for high heat flux thermal control.

EHD phenomena involve the interaction of electric fields and flowfields in a dielectric fluid medium. This interaction can induce flow motion by electric body force. The electric body force density f_e acting on the fluid molecules can be expressed as follows [8]

$$f_e = qE - \frac{1}{2}E^2\nabla\varepsilon + \frac{1}{2}\nabla\left[E^2\left(\frac{\partial\varepsilon}{\partial\rho}\right)_T\rho\right] \quad (1)$$

where q is the charge density, E is the electric field, ε is the fluid permittivity, ρ is the fluid density, and T is the fluid temperature. The first term represents Coulomb force, which is the force acting on the free charges in an electric field. The second and third terms represent the polarization force acting on polarized charges. The second term, the dielectrophoretic force, is associated with the electric permittivity gradient. It arises when the applied electric field induces a dipole due to the presence of polarizable particles or multiple phases in the working fluid. If the permittivity of the particle is higher than the surrounding medium, the EHD force acts in the way that the particle moves to the high field strength region. In the converse case, the EHD force acts toward the lower electric field strength region. The third term, the electrostriction term, is relevant only for compressible fluids. Thus, EHD pumps require either a free space charge or a gradient in permittivity within the fluid. In an isothermal single-phase liquid, $\nabla\varepsilon$ vanishes, resulting in Coulomb force as the only mechanism for generating a permanent EHD motion.

There are two main mechanisms for generating a space charge in an isothermal liquid. The first one is associated with the ion injection at a metal/liquid interface and the related pumping is referred to as ion-drag pumping. However, the ion-drag pumping is not desirable, as the injection of ions into the working fluid can deteriorate the fluid's electrical properties. Also, ion injection requires relatively higher electric fields that can result in a hazardous operation condition. The second mechanism for generating a space charge in an isothermal liquid is associated with the process of dissociation of the neutral electrolytic species and recombination of the generated ions [9]. Under relatively low electric fields, dissociation and recombination are in dynamic equilibrium,

$$A^+B^- \leftrightarrow A^+ + B^- \quad (2)$$

When an electric field exceeding a certain value (approximately 1 kV/cm, depending on the liquid characteristics) is applied, the rate of dissociation exceeds that of the recombination and it further increases at higher electric fields, thus generating a nonequilibrium layer where the dissociation-recombination reactions are not in equilibrium [10]. The charges generated by dissociation are redistributed in the region by the applied electric field, resulting in the heterocharge layers around the electrodes. Heterocharge means that the charge has the opposite polarity from that of the adjacent electrode. The thickness of the heterocharge layer is proportional to the corresponding relaxation time (defined as the ratio of electrical permittivity and conductivity, and represents the time during which a charged particle maintains its charge in a medium) of the working fluid τ and the strength of the local electric field. The attraction between the electrode and the charges within the heterocharge layer induces a fluid motion near the electrode from the liquid side to the electrode side. This type of pumping is referred to as the conduction pumping. Considering an electrode configuration as shown in Fig. 1, the strong electric fields build up the heterocharge layers around the electrodes. With this electrode configuration, the net axial motion around the ring ground electrode is almost canceled due to the geometric symmetry. Thus, the motion around the high-voltage electrode primarily contributes to the net axial flow. Because the electric field is high near the high-voltage electrode, the thickness of the corresponding heterocharge layer and the pressure across it will be high as well. Therefore, the flow direction will be from the ground electrode to the high-voltage electrode. The current vs voltage behavior in this regime is subohmic, showing only a slightly increased current with increased voltage. The details of the EHD conduction pumping mechanism can be found in Atten and Seyed-Yagoobi [9], Jeong and Seyed-Yagoobi [11–13], and Jeong et al. [14].

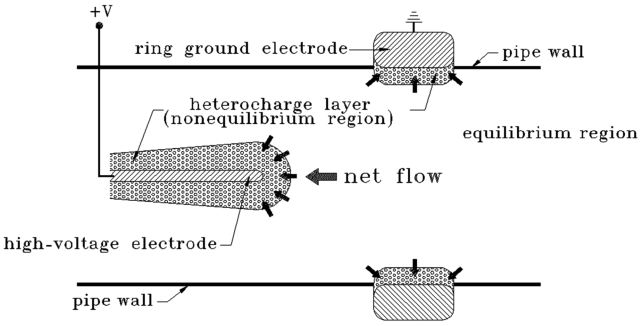

Fig. 1 Illustration of EHD conduction pumping mechanism [11–14].

The performance characteristics of an EHD conduction pump in two-phase loop are investigated in this paper. Specifically, two EHD conduction pump sets (EHD pump-1, EHD pump-2), consisting of six electrode pairs, were built and installed alternatively in two two-phase loops (EHD loop-1, EHD loop-2) with condenser and high heat flux evaporator. Deaerated HFC-134a and unprocessed HFC-134a are used as the working fluid to investigate the influence of noncondensable gas in fluid. Generated pressure by these EHD pumps, electric current, mass flow rate, and pressure drop across the evaporator are measured by varying the applied voltage, the sink temperature, and changing the working fluid. We report performance characteristics of the EHD conduction pump in two-phase loops such as the temperature dependence of EHD pump performance, effects of deaeration of working fluid, effects of electrode design, pressure loss within the EHD pump, and influence of the size of two-phase loops.

Fig. 2 High-voltage electrode of EHD conduction pum: a) cross section, b) EHD pump-1, c) EHD pump-2.

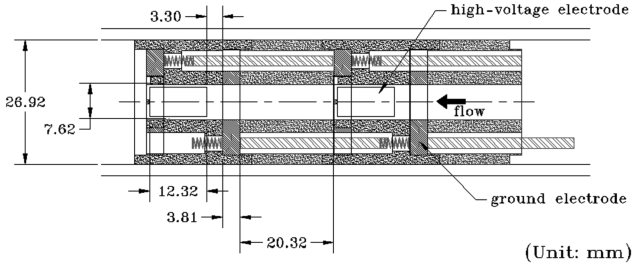

Fig. 3 Assembled high-voltage electrode and ground electrode (two pairs shown).

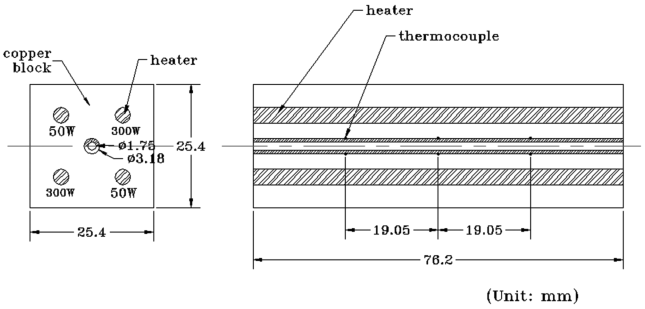

Fig. 5 Cross section of evaporator.

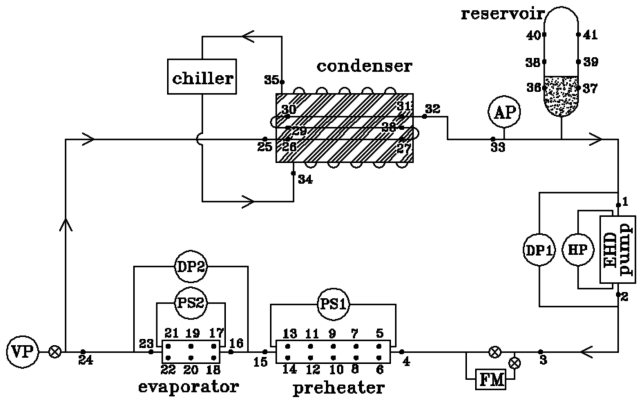

a) EHD Loop-1

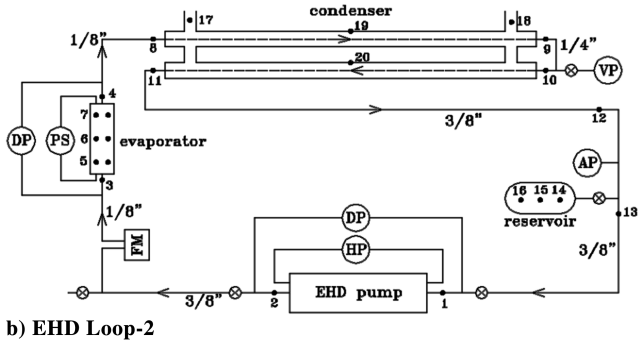

b) EHD Loop-2

Fig. 4 Experimental setup of the test loops with EHD conduction pump.

Experimental Apparatus

Electrohydrodynamic Conduction Pump

The EHD conduction pump consists of six electrode pairs; each pair containing one high-voltage electrode and one ground electrode. The high-voltage electrodes are fabricated from one large-radius tube and six small-radius tubes, whereas the ground electrodes are made as rings, flush against the pump inner wall. The high-voltage and ground electrodes are made of stainless steel. The cross section of the high-voltage electrode of the EHD conduction pumps is shown in Fig. 2a. The edges of the high-voltage electrode were coated with gold to remove/reduce any sharp edges. This reduces the occurrences of ion injection sites that compete with and reduce the pressure head generated from the conduction phenomena. Two EHD pumps (EHD pump-1 and EHD pump-2) were built. The picture of the high-voltage electrode of the EHD pump-1 and EHD pump-2 is shown in Figs. 2b and 2c, respectively. The geometric dimension of the two pumps are identical; however, EHD pump-2 represents an improved fabrication method that employs a smoothed electrode surface and set screws rather than the wrapped wires of EHD pump-1 to make the electrical connection between the electrode and the bus line. This technique also provided a more consistent distance between the high-voltage and ground electrodes. The assembled EHD conduction pump is shown in Fig. 3. The open cross-sectional area of the high-voltage electrode is an important performance parameter. Greater electrode projected area perpendicular to the axial flow induces stronger flow toward the high-voltage electrode. The electrode design is somewhat of an art as the projected electrode area must be great enough to promote a strong mass flow rate, but not so great as to restrict the flow due to large pressure drops.

Two-Phase Loop

The experimental setup of the two-phase loops (EHD loop-1 and EHD loop-2, respectively) with EHD conduction pump is illustrated in Figs. 4a and 4b. EHD loop-1 consists of EHD conduction pump, condenser, preheater, high heat flux evaporator, reservoir, and transport lines. The total length of the loop is approximately 10 m. The inner diameter of the transport lines is 8.1 mm. The preheater can be used to adjust the evaporator inlet temperature. The evaporator was incorporated in the loop to simulate high heat flux source in a laser application. A strip heater is attached to the reservoir to control the reservoir temperature that determines the saturation condition of the loop. EHD loop-2 basically has the same configuration with EHD loop-1 except in a smaller size with smaller tubing diameter, shorter transport lines, and no preheater section. The total length of EHD loop-2 is approximately 5.0 m. The diameter of the transport lines used in EHD loop-2 are 3.18, 6.35, and 9.53 mm, whereas 9.53 mm tubing is mostly used in EHD loop-1. The EHD loop-2 was built as a life test loop to investigate the performance over a long period of time (months or years). The reservoir temperature in both loops was set to 28°C for the entire test. The reservoir temperature should be set to a higher temperature than ambient temperature to secure the full charge of the working fluid along the loop. To minimize the heat loss to surroundings, the entire experimental apparatus was wrapped with insulation materials. Heat loads were supplied to the evaporator through the cartridge heaters inserted into the copper block

Table 1 Bias limits and precision limits

Bias limit	Precision limit (high-voltage supply between 10 and 20 kV)
Temperature measurement, ±0.5 K	differential pressure, 0.7 ~ 11.9%
Voltage of high-voltage supply, 2.0%	mass flow rate, 0.6 ~ 23.3%
Current of high-voltage supply, 1.5%	
Voltage of evaporator heater, 2.0%	
Current of evaporator heater, 2.5%	
Differential pressure, 0.5%	
Mass flow rate, 3.5%	
Evaporator inner diameter, ±15.0%	

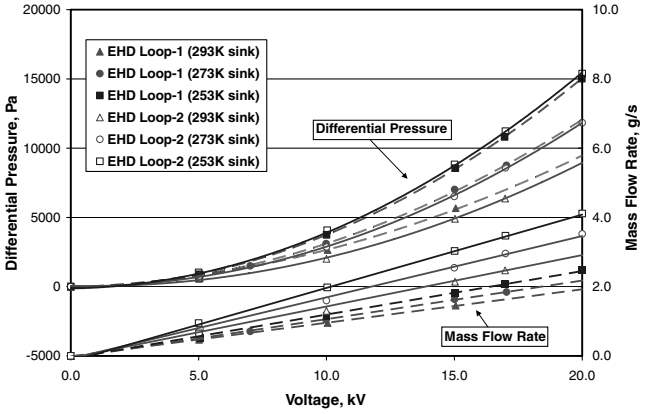

Fig. 6 Pressure generation and mass flow rate of EHD pump-2 as a function of applied voltage with various sink temperatures (unprocessed HFC-134a used).

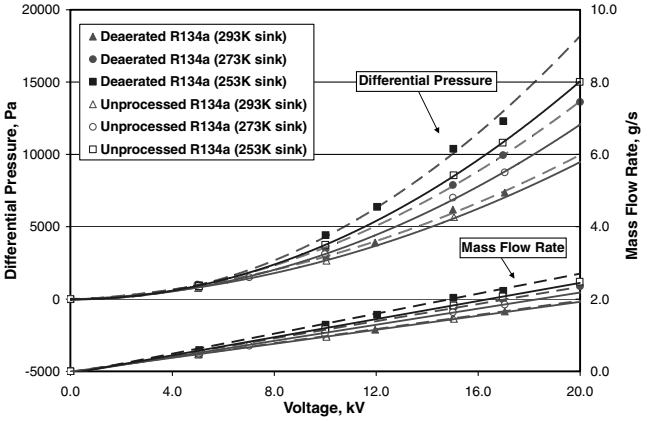

Fig. 7 Pressure generation and mass flow rate of EHD pump-2 as a function of applied voltage with various sink temperatures for unprocessed and deaerated HFC-134a in EHD loop-1.

surrounding the pipe. T-type thermocouples (TC) located on the pipe surface at 19.05 mm intervals inside the copper block (three for the upper and three for the lower surface), as shown in Fig. 5. The heat was removed at the condenser that was connected to a recirculating chiller. The flow rate of the recirculating refrigerant through the loops was measured using a flowmeter from Micron Motion, Inc., installed before the preheater section in EHD loop-1 and before the evaporator section in EHD loop-2. The absolute pressure (AP) was measured at a location between the condenser and the reservoir via absolute pressure transducers. The differential pressures through the EHD conduction pump and the evaporator were also measured using a differential pressure transducer. The differential pressure transducer through the evaporator is dedicated for the measurement of boiling effect on the pressure drop.

Error Analysis

The uncertainty analysis was performed according to the American Society of Mechanical Engineers (ASME) "Policy on Reporting Uncertainties in Experimental Measurements and Results" [15,16]. The bias and precision limits obtained from the instrumental data, calibration, and measurement data are shown in Table 1. The absolute pressure transducer has $\pm 0.1\%$ of accuracy with $\pm 1.5\%$ total error of temperature effects for the range between -20 and 80°C.

Power consumption of the EHD pump is calculated from the applied voltage and current of the high-voltage power supply. The maximum uncertainty in power consumption is 5.0%. The total heat load of the evaporator is calculated from the voltage and current measured using a multimeter and heat flux is calculated using heat load and internal surface area of the evaporator. The uncertainty in heat load and heat flux is 5.1 and 15.9%, respectively. In the range of 10–20 kV of high-voltage supply, the uncertainty for differential pressure and mass flow rate is 0.9–12.0% and 2.9–23.6%, respectively. The uncertainty for differential pressure and mass flow rate is usually higher at lower applied voltage and higher sink temperature due to its smaller measurement values at that condition.

Results and Discussions

The authors executed a comprehensive test matrix to verify the operational characteristics of the EHD-based thermal control loop.

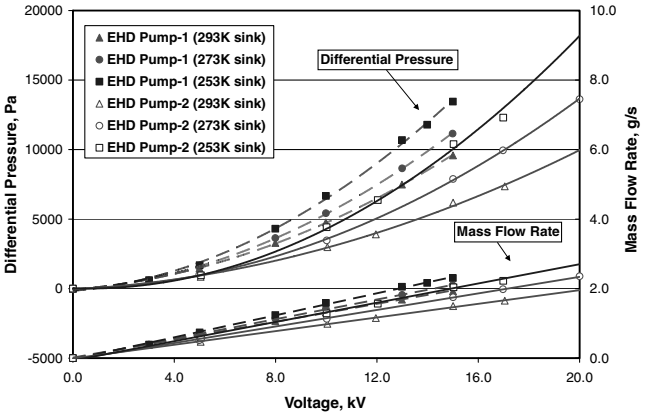

Fig. 8 Pressure generation and mass flow rate of EHD pumps 1 and 2 as a function of applied voltage with various sink temperatures in EHD loop-1 (deaerated HFC-134a used).

The experiments employed two test loops to examine architectural effects, two similar EHD pumps to validate the conduction mechanism, and deaerated and unprocessed working fluid to quantify the effects of noncondensable gases. The experiments were carried out in two categories: adiabatic case without energy transport, i.e., no heat load in the evaporator, and diabatic case with energy transport, i.e., a heat load in the evaporator. The performance characteristics of the two categories are accordingly described in the following description.

Adiabatic Case without Energy Transport

Temperature Dependence of EHD Pump Performance

The pressure generation and mass flow rate of EHD pump-2 as a function of applied voltage and sink temperature (293, 273, and 253 K) in EHD loop-1 and EHD loop-2 are presented in Fig. 6. The working fluid is unprocessed HFC-134a. The results show that pump performance has no dependence on loop configuration; that is, the

Table 2 Generated pressure and relaxation time of HFC-134a at the EHD pump operating temperatures in the case of EHD pump-2 operation in EHD loop-1 with unprocessed HFC-134a (EHD pump at 20 kV)

Sink temperature, K	EHD pump operating temperature, K	Generated pressure, Pa	Electrical permittivity, pF/m[a]	Electrical conductivity, S/m[a]	Relaxation time, ms
293	292.7	9444	93.82	3.87E-08	2.43
273	283.6	12,079	100.42	3.12E-08	3.22
253	269.3	15,010	111.60	2.80E-08	3.99

[a]Obtained from [17].

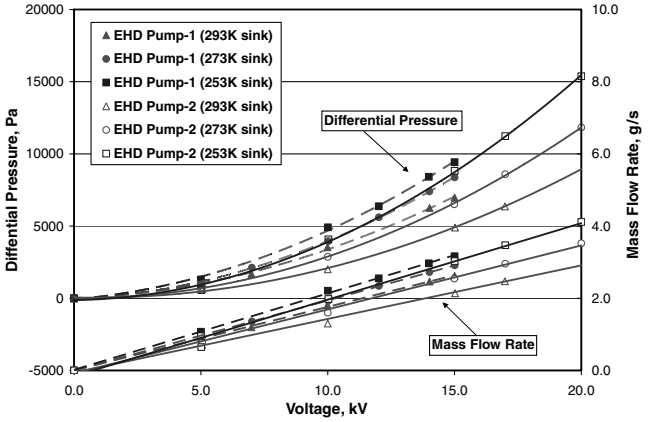

Fig. 9 Pressure generation and mass flow rate of EHD pumps 1 and 2 as a function of applied voltage with various sink temperatures in EHD loop-2 (unprocessed HFC-134a used).

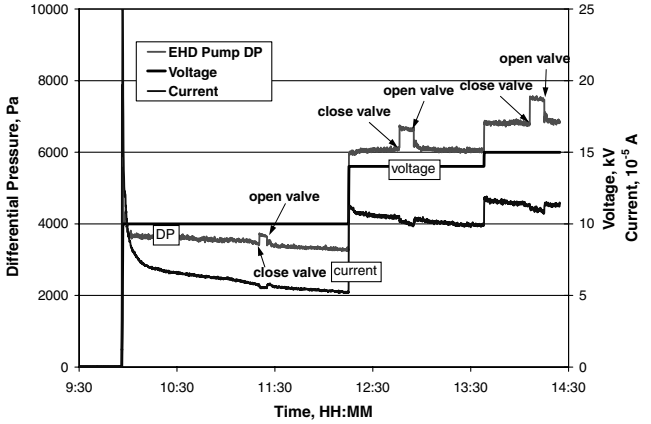

Fig. 10 Applied voltage, generated pressure head, and current at various applied voltages (10, 14, 15 kV) with valve closed/opened (EHD pump-1 in EHD loop-2, unprocessed HFC-134a).

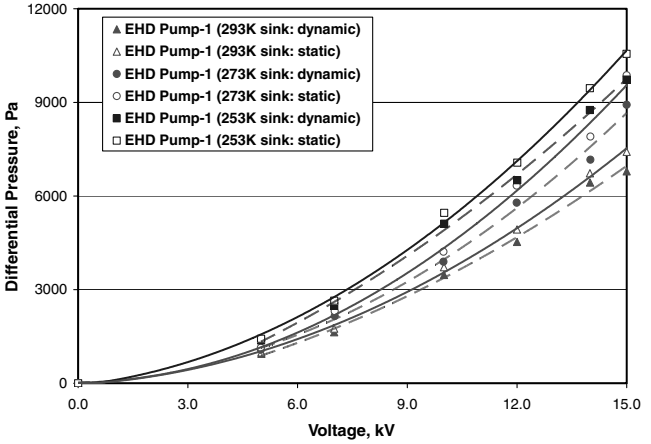

Fig. 11 Generated pressure head in static and dynamic cases as a function of applied voltage with various sink temperatures with EHD pump-1 in EHD loop-2 (unprocessed HFC-134a used).

small differences in pressure head generation are explained by small temperature differences in pump operating temperatures and applied voltages in the two loops. The mass flow rate is much higher in EHD loop-2 due to the shorter transport lines and subsequently smaller viscous pressure losses throughout that loop. One should note that the mass flow rate is linearly proportional to the applied voltage, whereas the pressure head has quadratic dependence on the applied

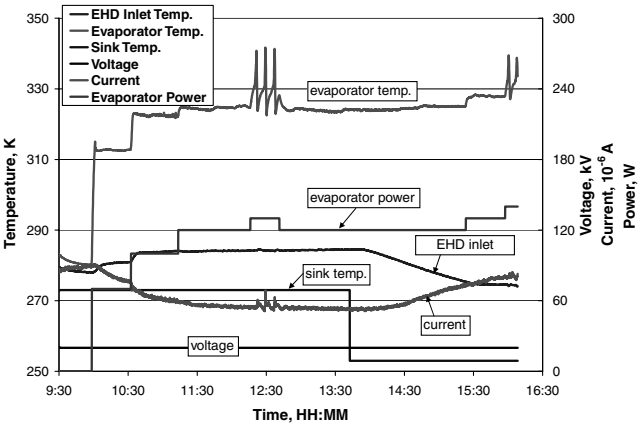

a)

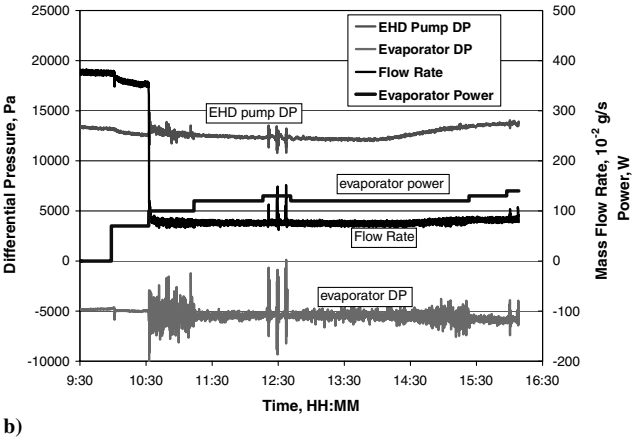

b)

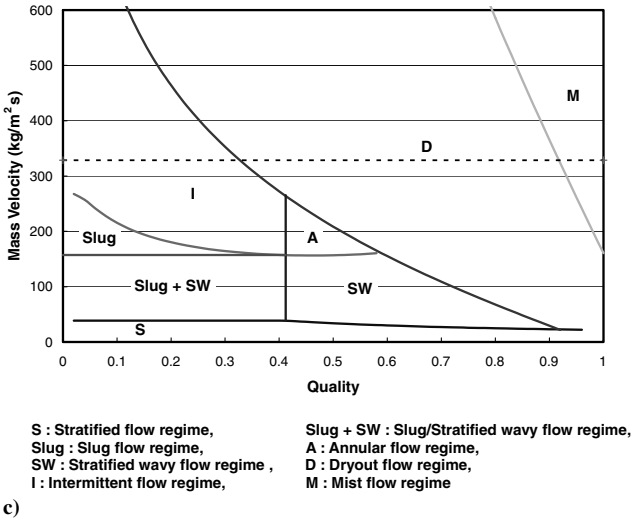

c)

Fig. 12 Time trend of performance parameters (a–b); c) flow pattern map at 100 W (EHD pump-2 in EHD loop-2, evaporator variation 70/100/120/130/120/130/140 W, deaerated HFC-134a).

voltage, implying that the pressure drop along the loop is approximately proportional to the velocity square.

The second result of note is that the generated pressure head increases as the sink temperature decreases. The lower sink temperature provides a lower temperature working fluid to the EHD pump; EHD pump pressure increases with decreasing temperature. This phenomenon can be explained in terms of relaxation time. The heterocharge layer thickness is proportional to relaxation time and electric field strength. At constant electric field strength, greater thickness of the heterocharge layer results in a larger generated pressure head. The data for the case of EHD pump-2 in EHD loop-1 using unprocessed HFC-134a illustrating this effect are presented in Table 2. We note that the generated pressure head and relaxation time

Table 3 Length of the subcooled region and vapor quality at thermocouple locations in the evaporator

		Quality, x[b]		
Heat load, W	X_{sat}, mm[a]	at $X = 19.05$ mm	at $X = 38.1$ mm	at $X = 57.15$ mm
70	24.92	0.000	0.077	0.188
100	12.02	0.065	0.242	0.419
120	8.28	0.132	0.364	0.597
130	7.05	0.170	0.439	0.709

[a] $X_{sat} = \dot{m}C_p(T_{sat} - T_{in})/(q \cdot \pi D_i)$
[b] $x(X) = \int_{X_{sat}}^{X} q\pi D_i \, dX$; $\dot{m}$ = mass flow rate, D_i = inner diameter, C_p = specific heat at constant pressure, T_{sat} = saturation temperature, T_{in} = evaporator inlet temperature, X = distance along the EV, h_{lv} = latent heat of vaporization

of the working fluid both increase as the EHD pump-operating temperature decreases. The increased ratio of the generated pressure approximately corresponds to the increased ratio of the relaxation time.

Effects of Deaeration of Working Fluid

The deaeration process first heated a reservoir tank filled with HFC-134a using a heat gun to release noncondensable gases. The tank was dipped in liquid nitrogen to condense and freeze the HFC-134a. Then, the noncondensed gas was evacuated. This process was carried out twice to enhance the deaeration. The amount of noncondensable gas, consisting primarily of air, in the unprocessed HFC-134a could reach 1.5% by volume [18]. Air that is mixed into the liquid phase can be a major problem for the EHD conduction pumping mechanism. The permittivity of air is less than HFC-134a, thus air bubbles in HFC-134a will move to the low electric field region, i.e., the ground electrode, by dielectrophoretic force. The bubble movement is in the opposite direction of the HFC-134a flow motion by the EHD conduction pump, thus reducing the generated pressure head relative to that of deaerated fluid. The data confirming this effect are presented in Fig. 7. At 20 kV applied voltage, the pressure heads generated in deaerated HFC-134a increased by 5.4, 12.8, and 23.3% compared with that of unprocessed HFC-134a for each sink temperature evaluated in this study. The effect of deaeration increased with an increase in applied voltage and decrease in sink temperature due to the following mechanism. The dielectrophoretic force is proportional to the electric field (i.e., applied voltage) and permittivity gradient as described in Eq. (1). The permittivity of HFC-134a increases as temperature decreases, whereas that of air is almost constant over the same temperature range. Therefore, the dielectrophoretic force [refer to Eq. (1)] increases with a decrease in sink temperature, increasing the deaeration effects. The noncondensable gas effects increase with decreasing size scale; thus, the presence of noncondensable gases can be disastrous at microscales. Noncondensable gas bubbles mixed in the working fluid can be trapped and accumulated in the EHD pumping section by dielectrophoretic force and surface tension, occupying the most part of the pumping section, leading to drastically reduced performance of the EHD conduction pump and causing the thermal control failure.

Effects of Electrode Design

The pressure generation and mass flow rate by the two EHD pumps in EHD loop-1 are presented in Fig. 8. The working fluid was deaerated HFC-134a for these experiments. We first examined the maximum voltage that could be applied to each pump: EHD pump-1 emitted sparks at 16 kV, whereas EHD pump-2 performed up to 22 kV. These results confirmed the improvements in design between the fabrication of EHD pump-1 and EHD pump-2. The best explanation for these results appears to be that some electrode pairs of EHD pump-1 might have shorter separation distance between the electrodes, due to the flexible wire connection between the high-voltage electrode and bus line. Furthermore, the presence of wires in EHD pump-1 yields relatively more sharp edges than EHD pump-2 allowing for more ion injection sites to compete with the conduction phenomena. We compared maximum pressure head generation and power consumption in each EHD pump at various temperatures. The maximum generated pressure heads are 9582, 11148, and 13447 Pa at 15 kV with EHD pump-1 and 9959, 13628, and 18501 Pa at 20 kV with EHD pump-2 at 293, 273, and 253 K sink temperature, respectively. The power consumption at these conditions is 3.09, 3.20, and 4.73 W for EHD pump-1 and 1.03, 1.97, and 5.02 W for EHD pump-2, respectively. The current used for the power consumption calculation was chosen after 30 min operation with the applied voltage. Note that the current usually decreases with time before it reaches an approximately settled value. The pressure generation and mass flow rate of EHD pump-1 and EHD pump-2 as a function of applied voltage with various sink temperatures in EHD loop-2 using unprocessed HFC-134a are presented in Fig. 9. The maximum pressure heads are 6976, 8372, and 9421 Pa at 15 kV with EHD pump-1 and 8991, 11831, and 15380 Pa at 20 kV with EHD pump-2 at 293, 273, and 253 K sink temperature, respectively. The power consumption at these conditions is 1.94, 2.46, and 2.74 W for EHD pump-1 and 0.96, 1.23, and 2.31 W for EHD pump-2, respectively. The results indicate that the EHD pump-2 is a better design providing higher pressure heads with lower power consumption. The superior design of EHD pump-2 showed even greater effects in EHD loop-2 using deaerated HFC-134a, in which a larger mass flow rate resulted in lower pump operating temperatures.

Pressure Loss Within EHD Pump

To investigate the pressure loss within the EHD pump section, the pressure heads of the static case (no flow motion, i.e., zero flow rate) and the dynamic case were measured with the outlet valve of the EHD pump closed/opened, respectively. To avoid the effects of temperature difference in pressure head generation, the pressure head was measured within 2 min after closing the outlet valve of the EHD pump. Temperature will increase with time after closing the valve because of Joule heating and parasitic heat exchange with ambient. This test was performed in EHD loop-2 using EHD pump-1 and unprocessed HFC-134a. The applied voltage, generated pressure of EHD pump, and current at 10, 14, and 15 kV with the valve closed and opened are presented in Fig. 10. The pressure head increases with the valve closed and decreases with the valve opened, whereas the current varies in the opposite way. The current increase in the open valve configuration represents the convection contribution to current flow. The generated pressure head in the static case and the dynamic case as a function of applied voltage at sink temperatures 293, 273, and 253 K are presented in Fig. 11. The pressure loss within the EHD pump increases with the applied voltage due to the higher velocity. The pressure loss within the EHD pump at 15 kV at 253 K sink temperature was 825 Pa. The pressure loss within the EHD pump diminishes the net pressure generation of the EHD pump. Therefore, the EHP pump design seeks to generate the greatest pressure while minimizing pressure loses through the pump. The pump design must optimize the projected area for the heterocharge layer to form vs pressure drop generated by reduced flow area. The pressure losses defined by the difference between the static and dynamic cases may not completely represent the flow losses in the pump, as the convection due to the flow of the working fluid influences the heterocharge layer distribution around the electrodes [12]. We have not investigated the magnitude of this effect during this study.

Diabatic Case with Energy Transport

Evaporator temperature (TC7), evaporator heat load, current, applied voltage, sink temperature, and EHD pump inlet temperature in EHD loop-2 with EHD pump-2 are presented in Fig. 12a. EHD

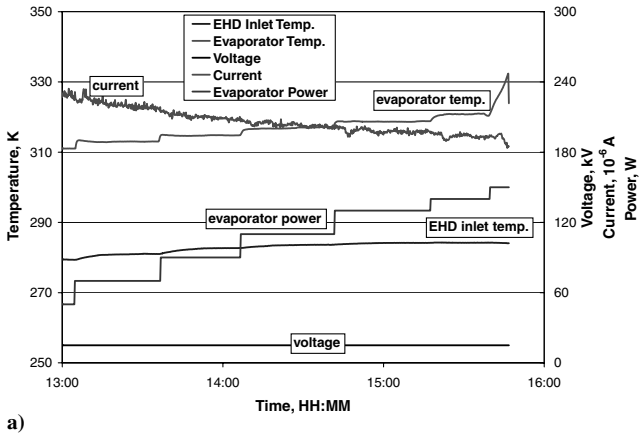

a)

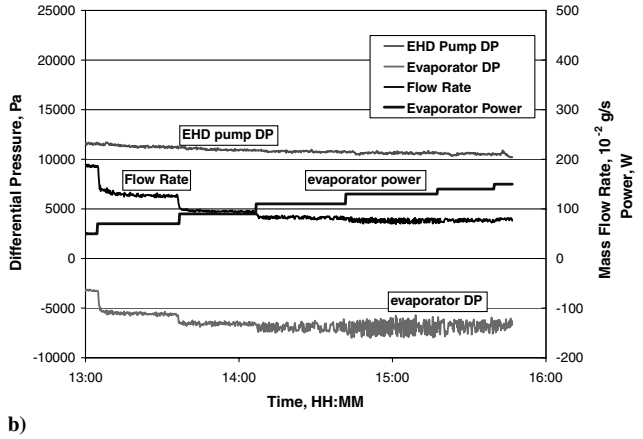

b)

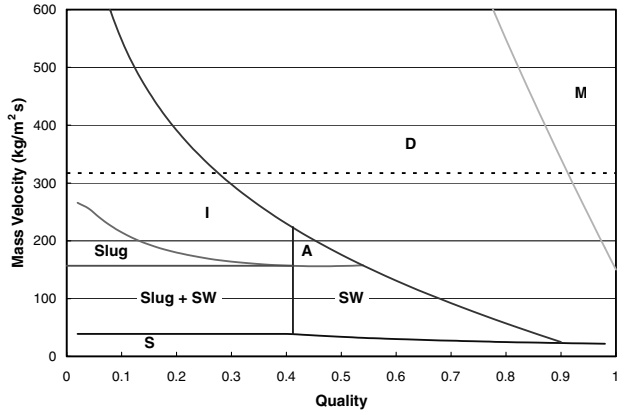

S : Stratified flow regime, Slug + SW : Slug/Stratified wavy flow regime,
Slug : Slug flow regime, A : Annular flow regime,
SW : Stratified wavy flow regime , D : Dryout flow regime,
I : Intermittent flow regime, M : Mist flow regime

c)

Fig. 13 Time trend of performance parameters (a–b); c) flow pattern map at 130W (EHD pump-1 in EHD loop-1, EHD pump at 15 kV, deaerated HFC-134a).

pump differential pressure (DP), evaporator DP, and mass flow rate are presented in Fig. 12b. The applied voltage was 20 kV, whereas the sink temperature varied from 273 to 253 K after confirming the maximum heat transport capability at 273 K. The evaporator heat load was varied from 70 to 130 W. After dryout occurred at 130 W with 273 K sink temperature, the evaporator power and sink temperature were reduced. Dryout can be easily recognized from rapid increase of the evaporator temperature to the maximum temperature of 340 K limited by a thermostat installed in the evaporator. The oscillation of evaporator temperature during dryout was caused by the cycling of the thermostat. The dryout at 273 K sink temperature was recovered when the heat load stepped down to 120 W. As illustrated in Fig. 12b, the mass flow rate rapidly dropped from 3.54 to 0.81 g/s and pressure drop through the evaporator oscillated approximately ±2000 Pa when the heat load was stepped up from 70 to 100 W. However, the average pressure drop across evaporator varied little between 70 and 100 W heat loads. This indicates that the pressure drop outside the evaporator section rapidly increased at 100 W due to high-velocity vapor flow. This is confirmed from the flow pattern map at 100 W ($q = 238663.5$ W/m^2, $G = 328.5$ kg/m^{2}s) based on the Wojtan–Ursenbacher–Thome flow pattern model [19] presented in Fig. 12c. The length of the subcooled region X_{sat} and the local vapor quality at thermocouple locations in the evaporator for each heat load is shown in Table 3.

As illustrated in Fig. 12c, the intermittent flow regime only exists at 70 W, whereas the flow regime changes from intermittent to dryout in the second half-region of the evaporator at 100 W, not experiencing annular flow regime due to large mass velocity. The large oscillation of pressure drop across the evaporator at 100 W appears to be due to the flow regime change. The oscillation reduces at 120 W because the dryout flow regime becomes dominant in the evaporator, stabilizing the boiling process. At 253 K sink temperature, the heat transport capacity increased to 130 W; this was expected, as the lower fluid temperature yields a higher pressure generation and mass flow.

The performance parameters of EHD pump-1 in EHD loop-1 at 273 K sink temperature are presented in Figs. 13a and 13b. Evaporator temperature (TC21), evaporator heat load, current, applied voltage, and EHD pump inlet temperature are presented in Fig. 13a. EHD pump DP, evaporator DP, and mass flow rate are presented in Fig. 13b. This test varied the heat load in the following steps: 20/30/50/70/90/110/130/140/150 W. Dryout occurred at 150 W. The flow pattern map at 130 W ($q = 310262.5$ W/m^2, $G = 317.3$ kg/m^{2}s), based on the Wojtan–Ursenbacher–Thome flow pattern model [19], is presented in Fig. 13c. The length of the subcooled region X_{sat} and the local vapor quality at thermocouple locations in the evaporator for each heat load is shown in Table 4.

The oscillation of the evaporator pressure drop begins to increase at 110 W maintaining approximately the same average pressure drop value. The mass flow rate decrease with heat load increase is relatively lower than that in the EHD loop-2 with EHD pump-2. Differences in loop dimensions appear to be responsible for these observations. The inner diameter of the transport line between the evaporator and condenser is approximately 1.75 mm in EHD loop-2 and 8.1 mm in EHD loop-1. The tube diameter between the evaporator and condenser has great influence on the pressure loss and mass flow rate in two-phase loop with dryout flow regime in the evaporator. In the dryout flow regime, the flow between the evaporator and the condenser has high-quality and velocity creating high pressure loss. This further explains the lower maximum heat transport capability in EHD loop-2 with EHD pump-2 at 20 kV vs EHD loop-1 with EHD pump-1 at 15 kV, even though the former has higher pressure head generation and mass flow rate compared with the latter. The maximum heat transport capabilities of EHD pump-1 in EHD loop-1 at 15 kV are 140 and 150 W, at 273 and 253 K sink temperature, respectively. Therefore, larger diameter transport lines between the evaporator and the condenser improve loop heat transport capability making transport line diameter an important loop optimization parameter. The efficiency of the EHD pump is defined as the ratio of power output and electric power input, i.e., $\text{Eff} = uA\Delta P/(VI)$ and the EHD pump has a low efficiency. However, note that the efficiency is not an important concern because the heat transport value is at least two orders of magnitude higher than the input electric power as illustrated in Fig. 12 and 13.

Conclusions

This presents the results of a project to characterize and quantify the performance of an EHD driven two-phase thermal control system using an EHD conduction pump. The experimental results indicate that both working fluid temperature and projected electrode area can significantly impact the generated pressure head. Lower EHD pump operating temperature and bigger projected electrode area provide a

Table 4 Length of the subcooled region and vapor quality at thermocouple locations in the evaporator

		Quality (x)		
Heat load, W	X_{sat}, mm	at $X = 19.05$ mm	at $X = 38.1$ mm	at $X = 57.15$ mm
70	28.83	0.000	0.030	0.092
90	14.34	0.027	0.135	0.244
110	9.11	0.080	0.233	0.387
130	6.66	0.128	0.324	0.520

higher generated pressure head by increased heterocharge layer thickness and area, respectively. Working fluid convection influences the development of the heterocharge layer, which in turn impacts the pump pressure generation capability. Quantifying this effect was beyond the scope of this work. Deaeration of the working fluid significantly enhanced the pressure generated by the EHD conduction pump. Please note that this phenomenon is specific to the conduction pumping technique; pumping by ion injection is likely enhanced by the presence of noncondensable gases. Improvements in the electrode design between the fabrication of EHD pump-1 and EHD pump-2 yielded performance improvements by reducing the number of sharp edges which lead to ion injection, which acts against the conduction phenomenon, and providing a consistent separate distance between the electrodes. Diabatic test results showed that the tube diameter between the evaporator and condenser has great influence on the pressure loss and mass flow rate in a two-phase loop with dryout flow regime in the evaporator. The larger diameter improves loop heat transport capability making the diameter an important loop optimization parameter.

Acknowledgments

This work was supported by National Research Council and NASA Goddard Space Flight Center Laser Risk Reduction Project.

References

[1] Butler, C., Ku, J., and Swanson, T., "Loop Heat Pipes and Capillary Pumped Loops: An Applications Perspective," *Space Technology and Applications International Forum (STAIF)*, Vol. 608, edited by M. S. El-Genk, American Inst. of Physics, Melville, NY, 2002, pp. 49–56.

[2] Jones, T. B., "Electrohydrodynamic Heat Pipes," *International Journal of Heat and Mass Transfer*, Vol. 16, No. 5, 1973, pp. 1045–1048. doi:10.1016/0017-9310(73)90043-4

[3] Sato, M., Nishida, S., and Noto, F., "Study on Electrohydrodynamic Heat Pipe," *ASME JSES KSES International Solar Energy Conference, Part 1 of 2*, American Society of Mechanical Engineers, New York, 1992, pp. 155–160.

[4] Bryan, J. E., and Seyed-Yagoobi, J., "Heat Transport Enhancement of Monogroove Heat Pipe with Electrohydrodynamic Pumping," *Journal of Thermophysics and Heat Transfer*, Vol. 11, No. 3, 1997, pp. 454–460.

[5] Jeong, S. I., and Seyed-Yagoobi, J., "Performance Enhancement of a Monogroove Heat Pipe with Electrohydrodynamic Conduction Pumping," *ASME International Mechanical Engineering Congress and Exposition (IMECE)* [CD-ROM], American Society of Mechanical Engineers, IMECE2002-33531, 2002.

[6] Mo, B., Ohadi, M. B., Dessiatoun, M. M., and Cheung, K. H., "Startup Time Reduction in an Electrohydrodynamically Enhanced Capillary Pumped Loop," *Journal of Thermophysics and Heat Transfer*, Vol. 13, No. 1, 1999, pp. 134–139.

[7] Jeong, S. I., and Didion, J., "Thermal Control Utilizing an Electrohydrodynamic Conduction Pump in a Two-Phase Loop with High Heat Flux Source," *ASME International Mechanical Engineering Congress and Exposition (IMECE)*, International Mechanical Engineering Congress and Exposition Paper 2004-60210, Nov. 2004.

[8] Melcher, J. R., *Continuum Electromechanics*, MIT Press, Cambridge, MA, 1981.

[9] Atten, P., and Seyed-Yagoobi, J., "Electrohydrodynamically Induced Dielectric Liquid Flow Through Pure Conduction in Point/Plane Geometry," *IEEE Transactions on Dielectrics and Electrical Insulation*, Vol. 10, No. 1, 2003, pp. 27–36. doi:10.1109/TDEI.2003.1176555

[10] Zhakin, A. I., "Conduction Models in Dielectric Liquids," *Electrohydrodynamics*, edited by A. Castellanos, Springer Wien, New York, 1998, Chap. 6.

[11] Jeong, S. I., and Seyed-Yagoobi, J., "Experimental Study of Electrohydrodynamic Pumping Through Conduction Phenomenon," *Journal of Electrostatics*, Vol. 56, No. 2, 2002, pp. 123–133. doi:10.1016/S0304-3886(02)00058-X

[12] Jeong, S. I., and Seyed-Yagoobi, J., "Innovative Electrode Designs for Electrohydrodynamic Conduction Pumping," *IEEE Transactions on Industry Applications*, Vol. 40, No. 3, 2004, pp. 900–904. doi:10.1109/TIA.2004.827771

[13] Jeong, S. I., and Seyed-Yagoobi, J., "Fluid Circulation in an Enclosure Generated by Electrohydrodynamic Conduction Phenomenon," *IEEE Transactions on Dielectrics and Electrical Insulation*, Vol. 11, No. 5, 2004, pp. 899–910. doi:10.1109/TDEI.2004.1349796

[14] Jeong, S. I., Seyed-Yagoobi, J., and Atten, P., "Theoretical/Numerical Study of Electrohydrodynamic Pumping Through Conduction Phenomenon," *IEEE Transactions on Industry Application*, Vol. 39, No. 2, 2003, pp. 355–361. doi:10.1109/TIA.2003.808954

[15] Editorial Board of American Society of Mechanical Engineers, "Policy on Reporting Uncertainties in Experimental Measurements and Results," *Journal of Heat Transfer*, Vol. 115, No. 1, 1993, pp. 5–6.

[16] Abernathy, R. B., Benedict, R. P., and Dowdell, R. B., "ASME Measurement Uncertainty," *Journal of Fluids Engineering*, Vol. 107, No. 2, 1985, pp. 161–164.

[17] Bryan, J. E., "Fundamental Study of Electrohydrodynamically Enhanced Convective and Nucleate Boiling Heat Transfer," Ph. D. Dissertation, Dept. of Mechanical Engineering, Texas A&M Univ., College Station, TX, 1998.

[18] Anon., "2004 Standard for Specifications for Fluorocarbon Refrigerants," Air-Conditioning and Refrigeration Inst., ARI-STD 700-2004, Arlington, VA, 2004.

[19] Wojtan, L., Ursenbacher, T., and Thome, J. R., "Investigation of Flow Boiling in Horizontal Tubes, Part 1: A New Diabatic Two-Phase Flow Pattern Map," *International Journal of Heat and Mass Transfer*, Vol. 48, No. 14, 2005, pp. 2955–2969.